

Key Points:

- Optimal proxies for remotely sensed POC were explored using in situ data of optical and biogeochemical parameters
- A new POC algorithm for GOCI satellite inversion with improved accuracy was developed based on the optical classification of water types
- POC diurnal variations in different water types were revealed by GOCI satellite observations

Correspondence to:

F. Shen,
fshen@sklec.ecnu.edu.cn

Citation:

Wei, X., Shen, F., Pan, Y., Chen, S., Sun, X., & Wang, Y. (2019). Satellite observations of the diurnal dynamics of particulate organic carbon in optically complex coastal oceans: The continental shelf seas of China. *Journal of Geophysical Research: Oceans*, 124, 4710–4726. <https://doi.org/10.1029/2018JC014715>

Received 2 NOV 2018

Accepted 18 JUN 2019

Accepted article online 26 JUN 2019

Published online 9 JUL 2019

Satellite Observations of the Diurnal Dynamics of Particulate Organic Carbon in Optically Complex Coastal Oceans: The Continental Shelf Seas of China

Xiaodao Wei¹, Fang Shen^{1,2} , Yanqun Pan¹, Shuguo Chen^{3,4}, Xuerong Sun¹, and Yongchao Wang¹

¹State Key Laboratory of Estuarine and Coastal Research, East China Normal University, Shanghai, China, ²Institute of Eco-Chongming (IEC), Shanghai, China, ³Department of Marine Technology, Ocean University of China, Qingdao, China, ⁴Laboratory for Regional Oceanography and Numerical Modeling, Qingdao National Laboratory for Marine Science and Technology, Qingdao, China

Abstract The continental shelf seas of China (CSSC) broadly encompass the Bohai Sea, the Yellow Sea, and the East China Sea and exhibit highly variable optical properties. Accurate satellite estimates of particulate organic carbon (POC) remain challenging because optimal proxies for remotely sensed POC are largely obscure in these optically complex coastal waters. In this study, optical and biogeochemical data, including the particulate beam attenuation coefficient (c_p), particulate backscattering coefficient (b_{bp}), remote sensing reflectance (R_{rs}), POC, total suspended matter (TSM), and chlorophyll-*a* (Chl*a*), were collected over multiple seasons and years in the CSSC. We first classified the study area into three different water types with three different POC retrieval proxies: the TSM for high-TSM waters, Chl*a* for low-TSM waters, and R_{rs} ratio ($R_{rs}(490)/R_{rs}(555)$) for moderate-TSM waters. A composite POC algorithm using these three optimal proxies was then developed for Geostationary Ocean Color Imager (GOCI) satellite data (hereafter called the POC_CSSC algorithm). The validation results indicated that the accuracy of GOCI-derived POC was greatly improved with a mean relative error of 32.08%. Application of the POC_CSSC algorithm to GOCI data over a tidally impacted estuary demonstrated the robustness of the algorithm and that tides play different roles in the broad CSSC. More specifically, tides have the strongest influence on nearshore estuarine waters, regulating the progression of high-POC water masses from estuary to offshore environments, while offshore waters were the least influenced by tides with less variable, low POC concentrations.

1. Introduction

Particulate organic carbon (POC) plays a critical role in sinking carbon fluxes and the transport of elements into the deep ocean as part of the biological pump (Druffel et al., 1992; Hedges, 1992). POC contains both living and nonliving materials produced largely via the ingestion and metabolism of organisms (Parsons, 1975). Distribution and transport pathways of POC exert significant influences on biogeochemical models when evaluating marine organic carbon budgets and assessing marine carbon stocks over regional and global scales (Pan et al., 2014; Stramska & Cieszynska, 2015). In continental shelf seas where are greatly influenced by terrestrial material inputs and phytoplankton activities, POC concentrations appear to be significantly higher than those in open oceans (Zhou et al., 2008).

Stocks of POC over continental seas vary greatly due to differences in the input sources of materials, local primary production and respiration, transport processes, suspension and sinking, etc. Assessments of spatial and temporal variations over a large range of POC, however, are often limited by shipboard surveys due to the immense time and labor demands of these surveys and are therefore relatively scarce (Allison et al., 2010). Satellite remote sensing provides advantages for quantitatively estimating water optical properties such as chlorophyll-*a* (Chl*a*) and total suspended matter (TSM) concentrations, which can potentially be related to POC abundance at large spatial scales and over long time series (Le et al., 2017; Liu et al., 2014; Loisel et al., 2002; Pan et al., 2014). The sensor on board the Geostationary Ocean Color Imager (GOCI), the first ocean color geostationary satellite with hourly revisits, is able to monitor short-term oceanic processes (Ryu et al., 2011), which makes it a powerful tool for monitoring diurnal POC variations in coastal oceans.

A number of ocean color algorithms, including both empirical and semianalytical approaches, have been proposed for satellite POC estimates. One type of POC retrieval algorithm is based on biogeochemical parameters such as $Chla$, which is best suited as a proxy for POC in open-ocean waters, where POC originates mainly from phytoplankton and metabolites (Legendre & Michaud, 1999; Sathyendranath et al., 2009; Stramska & Stramski, 2005). However, in estuarine and nearshore coastal waters, POC is poorly correlated with $Chla$ and but is better associated with TSM due to the influences of terrigenous runoff (Hung et al., 2000; Hung et al., 2013; Zhu et al., 2006). The second type of POC retrieval algorithm is based on empirical relationships, for example, the relationship between POC and remote sensing reflectance (R_{rs}) data, such as the algorithm based on the blue-to-green (B-G) band ratio of R_{rs} (hereafter called the B-G algorithm; Stramska & Stramski, 2005; Stramski et al., 2008). The third type of POC retrieval algorithms are semiempirical algorithms (Stramski et al., 1999), which adopt a two-step strategy that first retrieves inherent optical properties (IOPs; e.g., the backscattering coefficient b_{bp} or beam attenuation coefficient c_p) based on the relationship between the IOPs and R_{rs} and then estimates POC based on the relationship between the POC and the IOPs (Gardner et al., 2006; Stramski et al., 1999). The main difference among these three types of algorithms is the type of optical proxy adopted for the POC inversion. At present, many different proxies, including the R_{rs} band ratio, b_{bp} , c_p , $Chla$ and TSM, are commonly used for remote sensing POC retrievals. A number of studies, however, have indicated that the relationships between POC and different proxies can greatly vary among water types and seasons, especially in variable, optically complex waters (Boss et al., 2015; Cai et al., 2015; Cetinić et al., 2012; Gardner et al., 2006; Hu et al., 2016; Hung et al., 2013; Le et al., 2017).

The continental shelf seas of China (CSSC) are typical Case 2 coastal waters with high turbidity, complex optical properties that are affected by the runoff of several large rivers (Shen et al., 2010; Ye et al., 2016; Yu et al., 2016), and varying sources of POC (Hung et al., 2013; Zhu et al., 2006). For example, turbid marginal seas contain more inorganic mineral particulates than offshore oceanic waters, and these highly refractive particulates have a substantial influence on the optical properties of turbid marginal seas (Shen et al., 2010). Therefore, it is difficult to use one general proxy for satellite ocean color to estimate POC in optically complex waters (Le et al., 2011; Loisel et al., 2013). One possible approach to cope with this challenge is to classify water into different types based on optical properties (Feng et al., 2005; Huang et al., 2014; Le et al., 2011; Lubac & Loisel, 2007; Moore et al., 2001) and then develop specific optimal proxies for each water type; this approach helps to improve the performance of ocean color algorithms in estimating the POC in optically complex waters. For instance, Huang et al. (2014) proposed an optical classification method and applied it to the retrieval of TSM and $Chla$ in highly turbid inland waters. This optical classification approach, however, remains less applicable for the retrieval of POC in coastal waters than in open-ocean waters. Furthermore, data on concurrent measurements of POC and bio-optical properties over the entire continental sea area of China are limited, and the relationships between POC and optical properties, as well as the mechanisms underlying these relationships, are not well documented (Wang et al., 2012). Thus, extensive field surveys on the spatial distribution of POC in the CSSC are clearly needed to better understand the POC dynamics therein and to develop ocean color algorithms using proper proxies for the POC in this area.

This study presents an extensive data set of in situ measurements, including biogeochemical (POC, $Chla$, and TSM) and optical parameters (c_p , b_{bp} , and R_{rs}). The main objectives of this study were to (1) explore the optimal optical proxies for the remote sensing of POC in the various types of optically complex waters of the CSSC, (2) develop a new ocean color POC algorithm based on an optical classification for GOCI satellite data, and (3) reveal the POC spatial distribution pattern in the CSSC and the diurnal POC variations in different water types from GOCI satellite observations.

2. Study Area and Data

The CSSC is located east of mainland China and consists mainly of three seas (the Bohai Sea, the Yellow Sea, and the East China Sea, encompassing an area of approximately 1.22×10^6 km²; Figure 1). The CSSC, one of the most productive marginal sea areas on Earth, is among the major global carbon reservoirs worldwide (Hung et al., 2003; Milliman & Meade, 1983), as it receives significant amounts of terrestrial inputs from the large Yangtze River and the Yellow River (Hung et al., 2003; Li et al., 2012; Wang et al., 2017; Zhou et al., 2008). Moreover, the CSSC is a highly dynamic system that extensively interacts with the Kuroshio

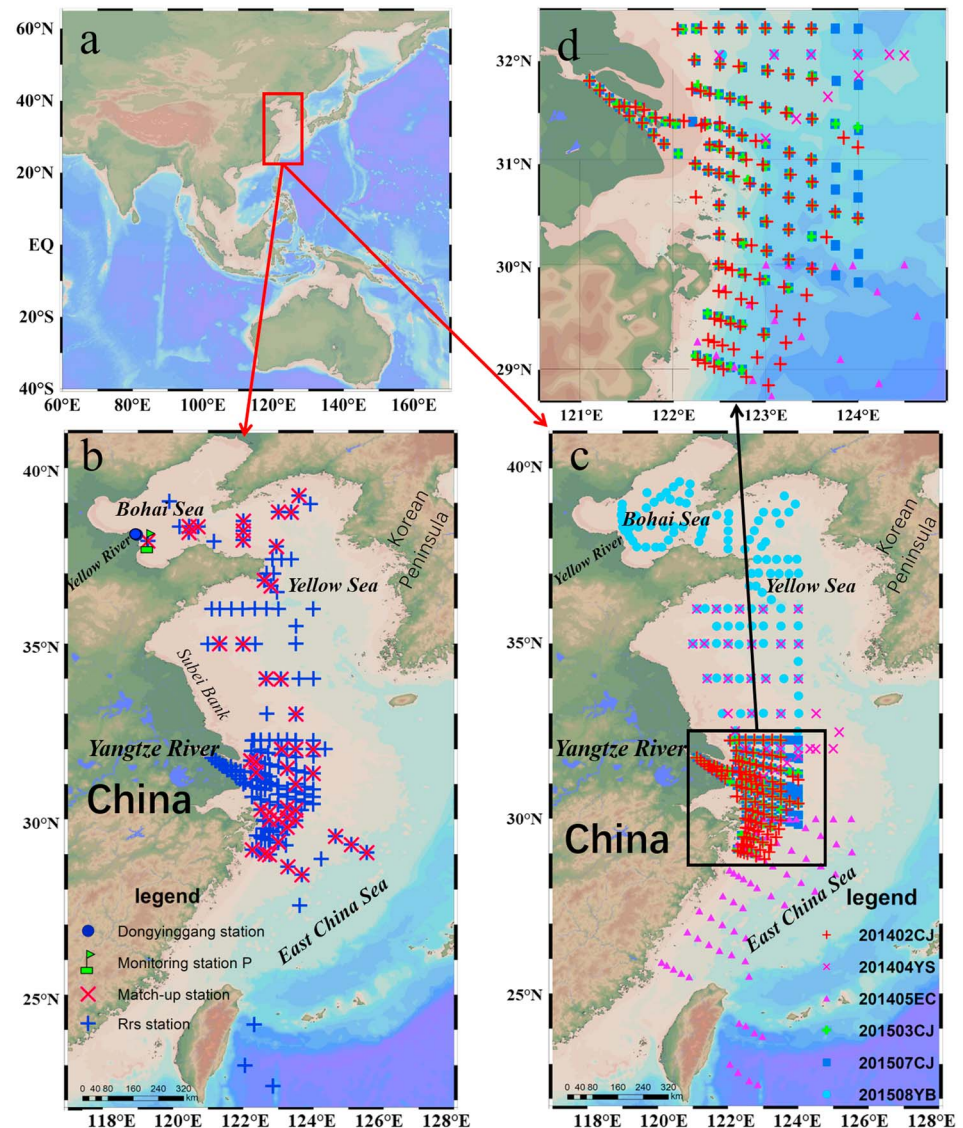


Figure 1. (a) Location of the continental shelf seas of China. (b) Field sampling stations that match the overpass of the Geostationary Ocean Color Imager (time window: ± 3 hr; matched stations are marked with a pink \times ; R_{rs} stations from which the in situ R_{rs} measurements were taken that were used to calibrate and validate the POC algorithm are marked with a blue +; the green flag indicates monitoring Station P in the Yellow River Estuary [coordinates: $37^{\circ}55.333'N$, $119^{\circ}17.001'E$; water depth: 13.5 m]; and the blue dot denotes the tidal elevation at the Dongyinggang tide gauge station). (c) Locations of the sampling stations during the six cruises (201402CJ [red +], 201404YS [pink \times], 201405EC [purple Δ], 201503CJ [green +], 201507CJ [dark blue \square], and 201508YB [light blue \circ]) with a magnified view of the Yangtze Estuary sampling stations provided in (d).

Current, the Taiwan Warm Current, the Yellow Sea Warm Current, and several alongshore currents; consequently, various source materials contribute to the optical complexity of the water in the CSSC (Chen, 2009; Hung et al., 2000; Zhang et al., 2016). Moreover, the optical properties of the water in the CSSC are further complicated by the influence of frequent algae blooms (green or red tides; Zhou et al., 2008; Liu et al., 2009; Shang et al., 2014; Tao et al., 2015).

Field data collection and water sampling broadly covering the CSSC were conducted during six comprehensive cruises over different seasons from 2014 to 2015 (Figure 1 and Table 1). To investigate the diurnal POC variations, we also conducted time series measurements at Station P (Figure 1b) in the Yellow River Estuary during 3–4 September 2015.

Table 1
Sample Information for the Six Cruises Conducted for This Study

Cruise no.	Date	Areas	Number of stations	Number of samples collected					
				POC	TSM	Chla	b_{bp}	c_p	R_{rs}
201402CJ	20 February to 12 March 2014	Yangtze Estuary and adjacent waters	94	94	94	94	79	82	43
201404YS	27 April to 7 May 2014	South Yellow Sea	34	34	34	25	20	31	23
201405EC	18 May to 13 June 2014	East China Sea	68	68	68	55	26	26	22
201503CJ	7–23 March 2015	Yangtze Estuary and adjacent waters	85	85	85	81	67	67	47
201507CJ	9–20 July 2015	Yangtze Estuary and adjacent waters	99	99	99	97	79	81	42
201508YB	17 August to 5 September 2015	Yellow Sea and Bohai Sea	113	132 ^a	132 ^a	131 ^a	125 ^a	132 ^a	31
Total			493	512	512	483	396	419	208

Note. POC = particulate organic carbon; TSM = total suspended matter.

^aIncludes data points from continuous observations.

2.1. Biogeochemical Data

In situ measurements of water optical properties were acquired during six comprehensive field campaigns in 2014 and 2015 (Figure 1c and Table 1). Surface water samples were collected using Niskin rosettes and filtered through 0.7- μm precombusted GF/F membranes (Whatman, USA) on board the ship under low pressure (i.e., a transmembrane pressure of 19.95 kPa). Sample membranes were stored in a refrigerator at -20°C . The laboratory analyses closely followed the Joint Global Ocean Flux Study measurement protocols (Knap et al., 1996). Briefly, sample membranes were dried at 50°C , acidified to remove carbonates (Hedges & Stern, 1984), and dried again for organic carbon content analysis using a Vario EL III CHONS elemental analyzer (Elementar, Germany). The concentrations of POC were calculated as the percentage of organic carbon multiplied by the sample mass and then divided by the volume of the filtered sample. An unused membrane was also subjected to all the steps of the analytical procedure, except for water sample filtration, and the result was used as a base value to be subtracted from the sample membrane results (Zhu et al., 2006).

We used 0.7- μm precombusted GF/F filters for TSM analysis. After sample filtration, the filters were rinsed with distilled water to remove salts and stored immediately in a refrigerator at -20°C . In the laboratory, each TSM sample membrane was dried to a constant weight and then measured using a Sartorius analytical balance (measurement accuracy: 0.1 mg, Germany). The mass of the TSM in each sample membrane was calculated by subtracting the mass of an unused membrane from the mass of the sample membrane with particulates. Then, the TSM concentration was calculated by dividing the mass of the TSM by the volume of the corresponding filtered water sample.

Chla samples were collected and analyzed following the Joint Global Ocean Flux Study measurement protocols (Knap et al., 1996). Briefly, a water sample (0.2–2 L) was filtered through a Whatman GF/F glass fiber membrane, and the membrane was folded immediately, covered with aluminum foil and subsequently transferred into liquid nitrogen. Later, in the laboratory, the Chla concentration was measured using a Hitachi F-4500 fluorescence spectrophotometer (Japan).

2.2. Optical Data

The optical data collected in this study included R_{rs} , c_p , and b_{bp} . In situ optical measurements and data post-processing were conducted following the National Aeronautics and Space Administration Ocean Optics Protocols (Fargion & Mueller, 2000). R_{rs} was measured using a sea surface hyperspectral surface acquisition system (Satlantic Co., Canada). This system consisted of three hyperspectral sensors that measured the incident solar radiance (L_t), incident skylight radiance (L_i), and downwelling spectral irradiance (E_d) at wavelengths ranging between 350 and 900 nm. L_t , L_i , and E_d over the target water were collected using the abovementioned water measurement method (Mobley, 1999). To avoid the effects of solar specular reflections, efforts were made to ensure that the azimuth angle of the observation plane of the target detector relative to the solar incidence plane was between 90° and 135° , and the zenith angle of the detector was maintained at 40° . More details can be found in Shen et al. (2014). R_{rs} was calculated using the following equation:

$$R_{rs} = L_w/E_d = (L_t - \rho L_i)/E_d \quad (1)$$

where ρ is the reflectivity of the air-water interface; ρ was calculated according to the Ruddick-Hojerslev model (Ruddick et al., 2006) based on the article published by Sokoletsky and Shen (2014).

Optical transmittance was measured using C-Star transmissometers with a central light source wavelength of 660 nm (± 20 nm; WetLabs Co., USA). During the 201402CJ, 201405EC, 201503CJ, and 201507CJ surveys, a C-Star transmissometer with an optical path length of 0.1 m was adopted. During the 201404YS and 201508YB surveys, a C-Star transmissometer with an optical path length of 0.25 m was used. The beam attenuation coefficient at 660 nm ($c(660)$) was calculated as follows:

$$c(660) = -l^{-1} \ln(Tr) \quad (2)$$

where l is the optical path length of the transmissometer ($l = 0.1$ or 0.25 m) and Tr is the optical transmittance measured. Furthermore, the particulate beam attenuation coefficient at 660 nm ($c_p(660)$) was calculated as follows:

$$c_p(660) = c(660) - c_w(660) - c_{CDOM}(660) \quad (3)$$

where $c_w(660)$ represents the beam attenuation coefficient of “pure seawater” at 660 nm. The transmittance of pure seawater at 660 nm was set to 91.3%, and $c_w(660)$ was approximately 0.364 m^{-1} (Fairall et al., 1996). The $c_{CDOM}(660)$ signifies the beam attenuation caused by colored dissolved organic matter (CDOM). In the red spectral range, the light attenuation caused by CDOM is approximately zero and therefore negligible (Bricaud et al., 1981). Equation (3) can be rewritten as follows:

$$c_p(660) = c(660) - 0.364 \quad (4)$$

The particulate backscattering coefficient, $b_{bp}(\lambda)$, was measured by an ECO-BB9 (WetLabs Co., USA) at 412, 440, 488, 510, 532, 595, 660, 676, and 715 nm during the 201402CJ, 201405EC, 201503CJ, 201507CJ, and 201404YS cruises or by a Hydroscat-6 (HOBILabs Co., USA) at 410, 442, 488, 532, 550, and 640 nm during the 201508YB cruise. The ECO-BB9 and Hydroscat-6 instruments recorded the total volume-scattering function in the backward direction at 117° and 140° , respectively (Maffione & Dana, 1997). These two instruments were calibrated before the measurements to confirm their performances within factory specifications. The $b_{bp}(\lambda)$ data were calibrated by the temperature-salinity correction (Zhang et al., 2009) and absorption correction (Sun et al., 2009) methods. To improve the accuracy of the backscattering measurements, we applied a sigma correction to the strong-absorption water data measured by the Hydroscat-6 (Wang et al., 2016). Further information on the processing procedure can be obtained in the ECO-BB9 User's Guide and Hydroscat-6 User's Guide.

2.3. In Situ Data at a Continuous Observation Station

To observe the diurnal POC dynamics and the biogeochemical and optical properties, 38-hr continuous measurements were made at monitoring Station P (Figure 1b) at the mouth of the Yellow River Estuary on 3–4 September 2015. Water samples were subsequently filtered and analyzed following the procedure in section 2.1. In this period, only GOCI imagery at 8:30–14:30 on 3 September 2015 was available for further analysis due to the cloud cover on 4 September 2015.

2.4. Satellite Data and Processing

GOCI Level 1b zenith radiance data were obtained from the Korea Ocean Satellite Center website (http://kosc.kiost.ac.kr/eng/p10/kosc_p11.html) and subjected to an atmospheric correction to generate sea surface Level 2 R_{rs} data. Due to differences in water turbidities throughout the CSSC, a top-of-atmosphere reflectance of 0.027 at 412 nm was used as the threshold to differentiate clear and turbid waters. The improved spectral optimization algorithm for atmospheric correction proposed by Pan et al. (2017) was adopted for turbid waters, whereas the algorithm based on the near-infrared “black pixel” assumption proposed by Gordon and Wang (1994) was adopted for clear waters. Furthermore, the TSM products were derived from GOCI R_{rs} data by implementing the semiempirical radiative transfer (SERT) algorithm (Shen, Verhoef, et al., 2010):

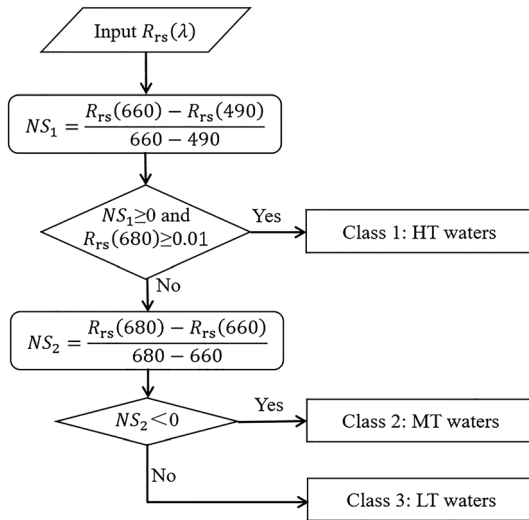


Figure 2. Flowchart of the optical classification of water types. The parallelograms (\square) and the rectangles (\square) represent inputs and outputs, respectively. The rhombi (\diamond) and the file rectangles (\square) represent diagnostic analysis and equations of optical classification, respectively. TSM = total suspended matter; HT = high-TSM; MT = moderate-TSM; LT = low-TSM.

$$\text{TSM} = \frac{(2\alpha/\beta)R_{rs}}{(\alpha - R_{rs})^2} \quad (5)$$

where α and β are wavelength-dependent coefficients, which can be calculated based on the article published by Shen et al. (2014). The Chla products from the Yellow Sea Large Marine Ecosystem Ocean Color Work Group (YOC) algorithm (Siswanto et al., 2011) were determined as follows:

$$\text{Chla} = 10^{(0.342 - 2.511 \log_{10} R - 0.277 (\log_{10} R)^2)} \quad (6)$$

where

$$R = \left(\frac{R_{rs}(443)}{R_{rs}(555)} \right) \left(\frac{R_{rs}(412)}{R_{rs}(490)} \right)^{-1.012} \quad (7)$$

Masks were applied to pixels on the GOCI imagery within a 3×3 extracted pixel array centered at the sampling stations if any of the following flags were set according to Bailey and Werdell (2006): atmospheric correction failure, land, sun glint, cloud or ice, high top-of-atmosphere radiance, low normalized water-leaving radiance at 555 nm, or stray light. Matchup data were taken from the GOCI satellite products (i.e., R_{rs} , TSM, and Chla) and concurrent in situ measurements. The time window was constrained within ± 3 hr. The matchups used for validation were chosen if the number of valid pixels after the application of flags was

> 4 and if the coefficients of variation for R_{rs} at 443, 490, and 555 nm were $< 0.2 \text{ sr}^{-1}$ (Melin et al., 2011). GOCI R_{rs} values were then calculated as the averages of the valid pixels in the 3×3 pixel arrays, and the GOCI- R_{rs} data used to derive the POC concentrations were derived using the algorithms developed in this study (section 3.2).

3. Methods

3.1. Optical Classification of Water Types

In this study, we used an approach similar to that proposed by Le et al. (2011) and Huang et al. (2014) to classify the waters in the CSSC into different types using the normalized slope (NS) criteria (hereafter NS criteria). Basically, the NS values of all 208 $R_{rs}(\lambda)$ samples were first calculated and then classified using the criteria stated below. $R_{rs}(\lambda)$ values at GOCI wavebands of 490, 660, and 680 nm were highly correlated with POC concentrations and therefore could be used to calculate the NS for the optical classification of water types. Specifically, backscattering by suspended particles is high in the 490 nm waveband, so this wavelength is often used to determine TSM concentrations (He et al., 2013); similarly, the 660-nm waveband usually contains Chla fluorescence signals, and the 680-nm waveband is generally associated with a reflection peak from Chla, so these wavelengths are often used to determine Chla concentrations (Le et al., 2011; Shen et al., 2010). Accordingly, two NS variables (NS_1 and NS_2) were calculated as follows:

$$NS_1 = (R_{rs}(660) - R_{rs}(490)) / (660 - 490) \quad (8)$$

$$NS_2 = (R_{rs}(680) - R_{rs}(660)) / (680 - 660) \quad (9)$$

The $R_{rs}(\lambda)$ spectra were therefore grouped into three classes by the optical classification of water types using these two NS variables (Figure 2). Class 1 (Figure 3b) was defined by $NS_1 \geq 0$ and $R_{rs}(660) \geq 0.01 \text{ sr}^{-1}$. The $R_{rs}(\lambda)$ spectra in Class 1 have broad and flat peaks from 550 to 700 nm due to strong backscattering by numerous suspended particles and can be related to waters with high TSM concentrations (Shen, Salama, et al., 2010).

If $NS_1 < 0$ or $R_{rs}(660) < 0.01$, the $R_{rs}(\lambda)$ spectra were defined as either Class 2 (Figure 3c) or Class 3 (Figure 3d). In moderately turbid waters with suspended solids and algal particles, $R_{rs}(680)$ might be

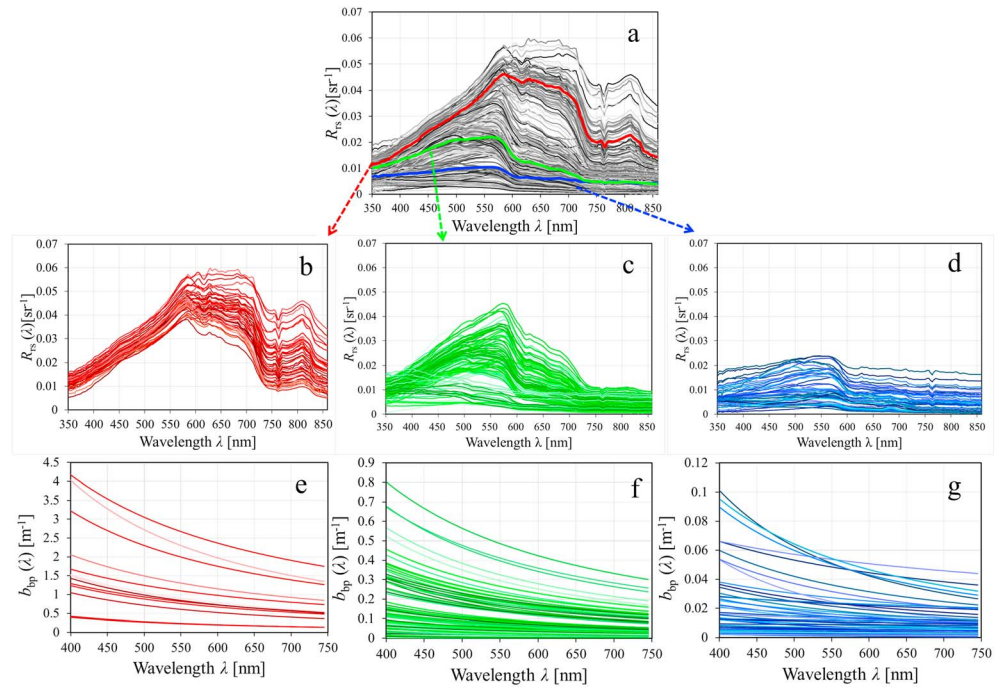


Figure 3. (a) $R_{rs}(\lambda)$ spectra collected in the continental shelf seas of China ($n = 208$); (b) optical Class 1 spectra for high-total suspended matter waters ($n = 46$); (c) optical Class 2 spectra for medium-total suspended matter waters ($n = 105$); (d) optical Class 3 spectra for low-total suspended matter waters ($n = 57$). In (a), the mean R_{rs} spectra are indicated by red lines for Class 1, green lines for Class 2 and blue lines for Class 3. (e) $b_{bp}(\lambda)$ spectra for Class 1 ($n = 12$); (f) $b_{bp}(\lambda)$ spectra for Class 2 ($n = 95$); (g) $b_{bp}(\lambda)$ spectra for Class 3 ($n = 49$).

higher than $R_{rs}(660)$ (i.e., $NS_2 \geq 0$) due to the absorption by algae at 660 nm and the contributions of fluorescence and scattering from algae and solids at 680 nm. Then, Class 2 waters, which were defined by $NS_2 < 0$, were further distinguished from Class 3 waters, which were characterized by $NS_2 \geq 0$. Figures 3c and 3d show that the Class 2 $R_{rs}(\lambda)$ spectra exhibit a single-peak pattern near 575 nm, while the Class 3 $R_{rs}(\lambda)$ have a relatively low order of magnitude in the full band range ($R_{rs}(\lambda) \leq 0.025 \text{ sr}^{-1}$).

Table 2
Correlations Between the POC Concentration and the Biogeochemical and Optical Parameters for Various Water Types Throughout the CSSC

Water type	Correlation	R^2	n
HT waters	$POC = 5.06 \times TSM + 37.33$	0.82	46
	$POC = 408.33 \times Chla^{0.028}$	0.001	46
	$POC = 8.39 \times c_p(660) + 140.46$	0.63	12
	$POC = 179.14 \times b_{bp}(555) + 74.7$	0.79	12
	$POC = 112.55 \times [R_{rs}(490)/R_{rs}(680)]^{-3.98}$	0.67	46
MT waters	$POC = 2.64 \times TSM + 66.91$	0.28	105
	$POC = 105.51 \times Chla^{0.28}$	0.25	103
	$POC = 13.71 \times c_p(660) + 58.06$	0.35	100
	$POC = 245 \times b_{bp}(555) + 77.47$	0.22	95
	$POC = 87.30 \times [R_{rs}(490)/R_{rs}(555)]^{-2.04}$	0.65	105
LT waters	$POC = -4.76 \times TSM + 187.76$	0.02	57
	$POC = 69.9 \times Chla^{0.63}$	0.72	57
	$POC = 109.97 \times c_p(660) + 16.22$	0.52	53
	$POC = 5403.23 \times b_{bp}(555) + 91.92$	0.30	49
	$POC = 83.79 \times [R_{rs}(490)/R_{rs}(555)]^{-3.75}$	0.63	57

Note. Results with the highest R^2 (coefficient of determination) are marked in bold. CSSC = continental shelf seas of China; POC = particulate organic carbon; TSM = total suspended matter.

The spectra of the particulate backscattering coefficients ($b_{bp}(\lambda)$) displayed pronounced differences in magnitude among the three water type classes (Figures 3e–3g), implying that the suspended particle content differed among the three classes. Indeed, the $b_{bp}(555)$ values were highly variable among the three water classes with an average $b_{bp}(555)$ of 1.381 m^{-1} for the high-TSM (HT) waters and average $b_{bp}(555)$ values of 0.099 and 0.016 m^{-1} for the moderate-TSM (MT) and low-TSM (LT) waters, respectively, determined from in situ measurements. Therefore, the waters could be grouped into Class 1 HT waters with an average TSM of 94.66 mg/L , Class 2 MT waters with an average TSM of 13.92 mg/L , and Class 3 LT waters with an average TSM of 4.17 mg/L .

3.2. Development of the POC Retrieval Algorithm

To find the best proxy for remotely sensed POC for each of the three different water types, we investigated the POC and biogeochemical and optical parameters, including the TSM, Chla, $R_{rs}(\lambda)$, $b_{bp}(555)$, and $c_p(660)$, through in situ measurements. Statistical analysis showed that the POC and TSM had the most significant correlation with $R^2 = 0.82$ in HT waters (Table 2 and Figure 4a); therefore, TSM was used as the proxy for estimating the POC in this water type. For LT waters, the most significant

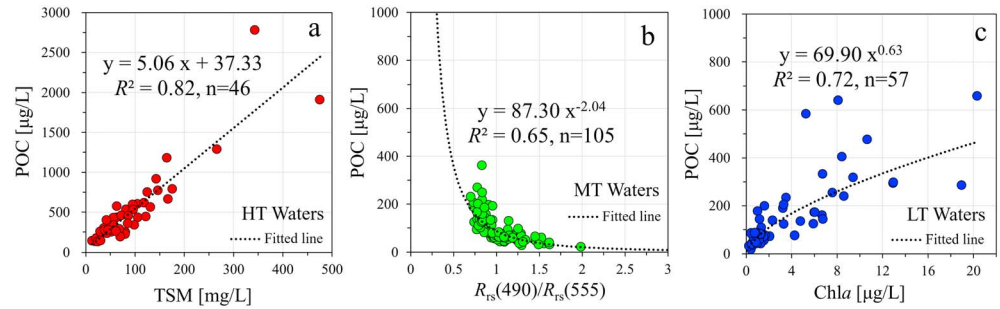


Figure 4. Relationships between the POC concentrations and the optimal proxies for the three water types from in situ data. (a) POC versus TSM for HT waters, (b) POC versus $R_{rs}(490)/R_{rs}(555)$ for MT waters, and (c) POC versus Chla for LT waters. POC = particulate organic carbon; TSM = total suspended matter; HT = high-TSM; MT = moderate-TSM; LT = low-TSM.

correlation was observed between POC and Chla ($R^2 = 0.72$; Table 2 and Figure 4c), and thus, Chla was the best proxy for estimating the POC in Class 3 waters. However, in MT waters, the correlations between the POC concentration and TSM, Chla, $b_{bp}(555)$, and $c_p(660)$ were relatively low ($R^2 = 0.28, 0.25, 0.35$, and 0.22 , respectively; Table 2). Instead, the $R_{rs}(490)/R_{rs}(555)$ band ratio appeared to have the most significant correlation with POC ($R^2 = 0.65$; Table 2 and Figure 4b).

Therefore, an algorithm (hereafter named the POC_CSSC algorithm) was proposed for GOCI POC estimates as follows using different proxies for estimating the POC in the optically complex waters of the CSSC based on the optical classification of water types:

$$POC = \begin{cases} 5.06 \times TSM + 37.33, & \text{for HT waters} \\ 87.30 \times [R_{rs}(490)/R_{rs}(555)]^{-2.04}, & \text{for HT waters} \\ 69.9 \times Chla^{0.63}, & \text{for HT waters} \end{cases} \quad (10)$$

The Pearson correlation coefficient (r), the coefficient of determination (R^2), the mean absolute error (MAE), the mean relative error (MRE), and the root-mean-square error (RMSE) were used to evaluate the performance of the algorithms. The equations for calculating these statistics are as follows:

$$MAE = \left[\frac{1}{N} \sum_{i=1}^N |X_{i,R} - X_{i,M}| \right] \quad (11)$$

$$MRE = \left[\frac{1}{N} \sum_{i=1}^N \left| \frac{X_{i,R} - X_{i,M}}{X_{i,M}} \right| \right] \times 100 \quad (12)$$

$$RMSE = \left[\frac{1}{N} \sum_{i=1}^N (X_{i,R} - X_{i,M})^2 \right]^{1/2} \quad (13)$$

where X is the POC, TSM or Chla concentration, N is the number of samples, and the subscripts R and M indicate estimated and measured variables, respectively.

In this work, the TSM in equation (10) was estimated by using the SERT algorithm proposed by Shen, Verhoef, et al. (2010), and the Chla in equation (10) was estimated with the YOC algorithm proposed by Siswanto et al. (2011). We used in situ data to validate the effectiveness of the abovementioned algorithms. Figure 5 shows the in situ data and estimated data for the TSM estimated from the SERT algorithm, the Chla estimated from the YOC algorithm and the POC estimated from the POC_CSSC algorithm. The in situ measurements and estimated values were distributed evenly along the 1:1 line with $RMSE = 37.23$ mg/L, $MAE = 63.19$ mg/L, and $MRE = 43.34\%$ for TSM (Figure 5a); $RMSE = 2.91$ μ g/L, $MAE = 4.54$ μ g/L, and $MRE = 117.83\%$ for Chla (Figure 5b); and $RMSE = 177.85$ μ g/L, $MAE = 74.83$ μ g/L, and $MRE = 30.89\%$ for POC (Figure 5c). These validation results indicate that the performance of the SERT algorithm proposed by Shen, Verhoef, et al. (2010) to retrieve TSM, the YOC algorithm proposed by Siswanto et al. (2011) to retrieve Chla and the POC_CSSC algorithm proposed in this work are acceptable for optically complex waters.

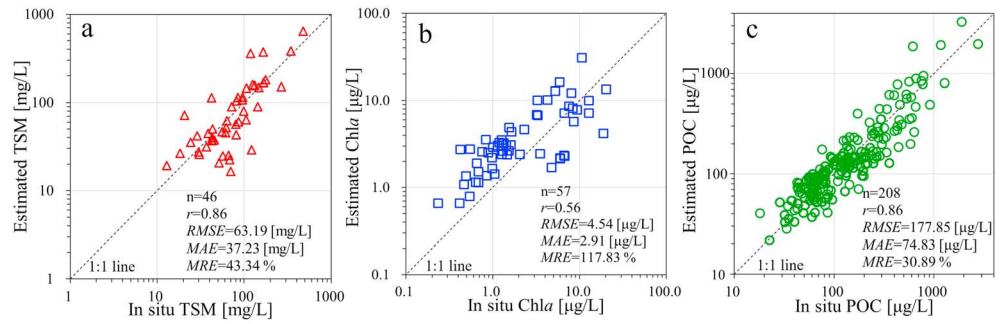


Figure 5. (a) In situ TSM versus TSM estimated by the semiempirical radiative transfer algorithm. (b) In situ Chla versus Chla estimated by the YOC algorithm. (c) In situ POC versus POC estimated by the POC_CSSC algorithm. POC = particulate organic carbon; TSM = total suspended matter; RMSE = root-mean-square error; MAE = mean absolute error; MRE = mean relative error.

3.3. Other Algorithms for POC Retrieval

Two algorithms, namely, the B-G algorithm by Stramski et al. (2008) and the maximum normalized difference carbon index (MNDCI) algorithm by Son et al. (2009), have been widely used to retrieve POC concentrations through remote sensing in global ocean waters. Using our in situ data set, the B-G algorithm was refined and rewritten as follows:

$$\text{POC} = 72.53 \times [R_{rs}(443)/R_{rs}(555)]^{-2.13}. \quad (14)$$

Similarly, by fitting the parameters in the MNDCI algorithm, the algorithm can be adjusted and rewritten as follows:

$$\text{POC} = 10^{(-294.6x^5 - 156.8x^4 + 11.22x^3 + 13.6x^2 + 2.403x + 1.877)}, \quad (15)$$

where

$$x = \frac{R_{rs}[555] - \max[R_{rs}[412], R_{rs}[443], R_{rs}[490]]}{R_{rs}[555] + \max[R_{rs}[412], R_{rs}[443], R_{rs}[490]]}. \quad (16)$$

In section 6.2, the GOCI-derived POC determined by the two main algorithms and POC determined by the proposed POC_CSSC algorithm using our matchups data set were applied to GOCI imagery and compared.

4. Application of the POC_CSSC Algorithm

4.1. Estimating POC From GOCI Data

The hourly GOCI-derived POC concentrations during the time period from 8:30 to 15:30 (local Beijing time) displayed a distinct spatial distribution (Figure 6). The highest POC values were observed in the Yangtze Estuary, Yellow River Estuary, and Subei Bank, which had GOCI-derived POC >500 $\mu\text{g/L}$; these high POC values might be due to the import of large amounts of terrestrial organic matter and the resuspension of particulate matter in the bottom water. The GOCI-derived POC concentrations then decreased in the middle shelf (e.g., from 500 to 80 $\mu\text{g/L}$). The lowest values were observed in the offshore East China Sea waters with GOCI-derived POC <80 $\mu\text{g/L}$; in this area, waters with low phytoplankton biomass (GOCI-derived Chla <0.4 $\mu\text{g/L}$) may be influenced by the oligotrophic waters of the Kuroshio and Taiwan Warm Currents.

4.2. Validation of GOCI-Derived POC

The 45 matchups between the GOCI overpasses and concurrent in situ data from the cruises were used for the validation of the GOCI-estimated POC concentrations from the POC_CSSC algorithm. The results show that the POC_CSSC algorithm gave good estimates of the GOCI-derived POC with $RMSE = 42.11$ $\mu\text{g/L}$, $MAE = 29.35$ $\mu\text{g/L}$, and $MRE = 32.08\%$ (Figure 7).

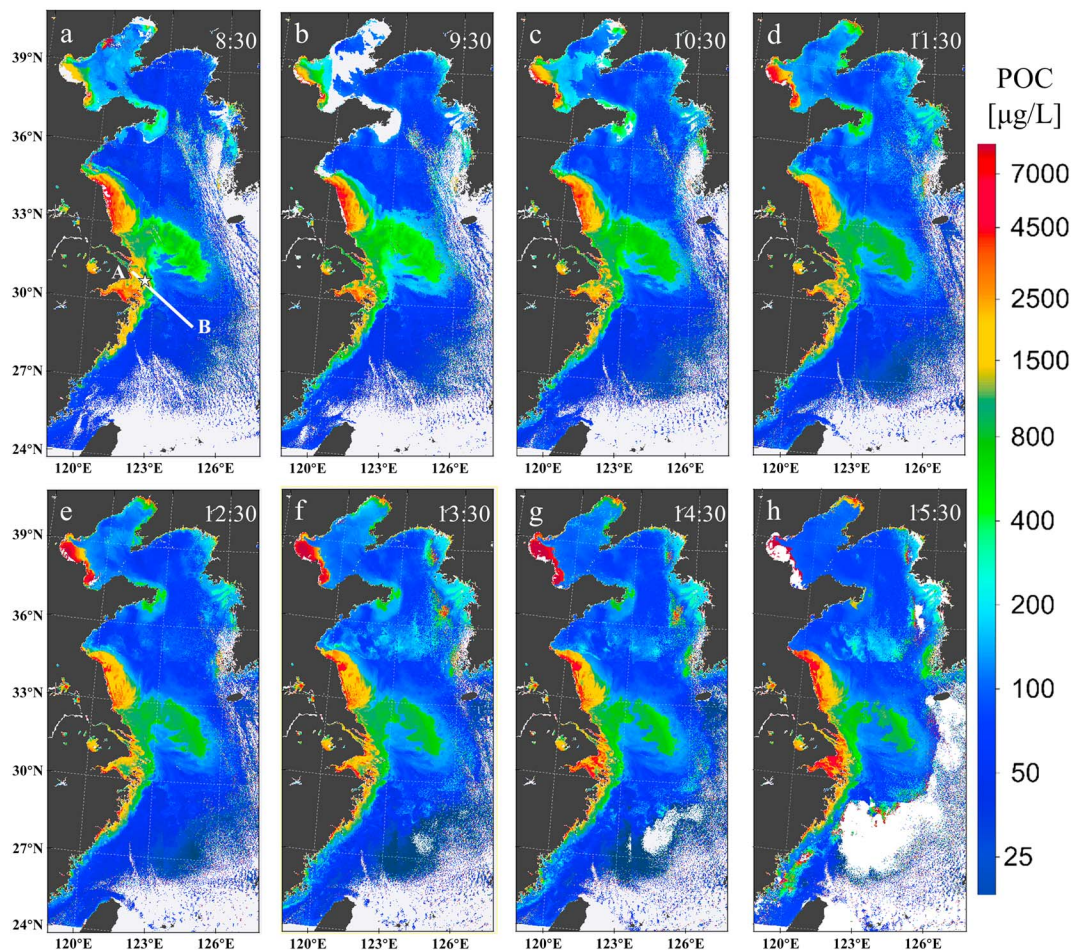


Figure 6. Geostationary Ocean Color Imager-derived POC imagery from the POC_CSSC algorithm for the time period of (a–h) 8:30–15:30 (Beijing time) on 7 April 2013, in the CSSC. To facilitate the discussion in section 5, a transect from the mouth of the Yangtze River Estuary (A) to the middle shelf of the CSSC (B) is shown in white (a). The white star marks the Lvhu tide gauge station. CSSC = continental shelf seas of China; POC = particulate organic carbon.

Moreover, the seven matchups between the GOCI overpasses and concurrent in situ data from the continuous observations at Station P presented a good consistency ($MAE = 16.57 \mu\text{g/L}$, $MRE = 15.29\%$), as shown in Figure 8. The GOCI-derived POC ($132.24 \mu\text{g/L}$) was higher than the in situ POC ($128.95 \mu\text{g/L}$) at 11:00 a. m. on 3 September 2015. Notably, although the GOCI-derived POC concentrations were slightly higher than the in situ POC concentrations, the two showed an overall similar pattern of variability.

5. Diurnal Variations of POC

To better understand the diurnal variations in the POC concentrations for the various water types distributed from nearshore to offshore regions, a transect from the mouth of the Yangtze River Estuary (A) to the middle shelf of the CSSC (B) was overlain onto the imagery of the GOCI-derived POC concentrations to better illustrate the different environmental forcings that drive POC variability in different water types (white line in Figure 6a). In Figure 9, the GOCI-derived POC concentrations along the transect gradually decrease from A to B. This transect may be divided into three sections corresponding to the three water types, i.e., a section from 122°E to 123°E for HT waters (Figure 9a), a section from 123°E to 124°E for MT waters (Figures 9a and 9c) and a section from 124°E to 125°E for LT waters (Figure 9d).

More specifically, Figure 9a shows that the hourly POC from 8:30 to 15:30 (e.g., on 7 April 2013) in the HT waters near the Yangtze River Estuary displayed a pronounced variation, which was impacted by tidal currents. During this time period, the water elevation recorded by the tidal gauge (white star in Figure 6a) was

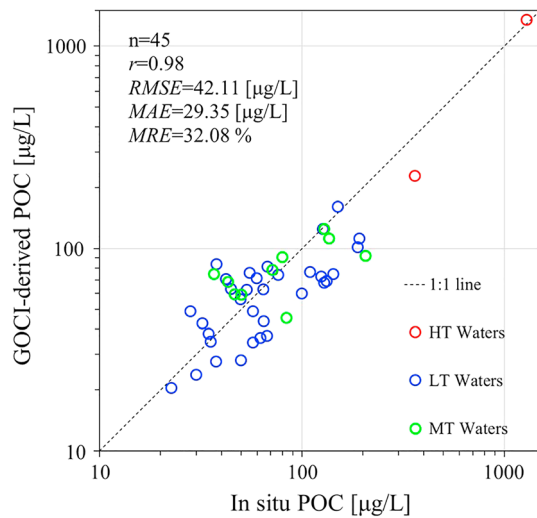


Figure 7. Validation of the GOCI-derived POC using the POC_CSSC algorithm developed in this study. Matchups from cruises for HT waters, MT waters, and LT waters are marked with red circles, green circles, and blue circles, respectively. GOCI = Geostationary Ocean Color Imager; POC = particulate organic carbon; TSM = total suspended matter; HT = high-TSM; MT = moderate-TSM; LT = low-TSM; RMSE = root-mean-square error; MAE = mean absolute error; MRE = mean relative error.

in an ebbing tidal stage (Figure 9b). Thus, all eight GOCI images were acquired during the ebb tide, when waters were flowing seaward to offshore areas in the Yangtze Estuary. With the influence of tidal currents, high POC concentrations nearshore moved southeastward to offshore areas, especially the turbidity front at the junction between the HT and MT waters (near 123°E, Figure 9a). Waters with extremely high TSM (250–400 mg/L) and POC (1,500–2,500 µg/L) values were in the section from 122.3°E to 122.5°E (Figure 9a), which corresponds to the maximum turbidity zone in the Yangtze Estuary. During the ebb tide stage, the high-TSM waters and the POC front drifted southeastward along the transect. As a result, in the HT waters of the nearshore area, the diurnal variation in the POC was relatively strong, and the tidal current was the dominant factor regulating this diurnal variation.

Figure 9c shows that the average POC concentration in the MT waters was approximately 100 µg/L. The hourly POC from 8:30 to 15:30 in the MT waters displayed a complicated diurnal variability. The POC concentration at 8:30 in the partial section was lower than that at 12:30 and 13:30 in the partial section (Figure 9c); this difference seemed to be related to sunlight. In addition, the hourly POC shifted slightly along the transect with the tidal current. The reason for these results could be that the POC in the MT waters was sourced from a mixture of detritus and phytoplankton particles, and the diurnal variations of POC were affected by multiple dynamic and environmental factors.

Figure 9d shows low POC concentrations in the LT waters with an average of 50 µg/L and less variability along the transect. The POC was lowest at 8:30 and increased gradually from 8:30 to 14:30 (Figure 9d) in this section, which seemed to be associated with sunlight. The POC concentrations in the LT waters had two small peaks near 124.45°E and 124.55°E coincident with an increase in Chl_a from 0.4 to 1 µg/L.

6. Discussion

6.1. Relationship Between POC and Proxy Parameters

In open oceans, where water optical properties are relatively uniform, POC originates mainly from phytoplankton, and $c_p(660)$ and $b_{bp}(555)$ are usually used as candidates for POC optical proxies (Stramski et al., 2008; Balch et al., 2010; Cetinić et al., 2012; Table 3). However, in coastal oceans, the components and concentrations of POC in waters are variable and impacted by terrestrial inputs, which leads to optical complexity, and it is difficult to choose an optimal optical proxy of POC. Our investigations showed that the relationships between POC and optical properties (e.g., $c_p(660)$ and $b_{bp}(555)$) in the CSSC are highly variable because of the optical complexity of the waters influenced by terrestrial sources and phytoplankton release. Table 3 shows that the optimal optical proxy of POC varied greatly among different water types in the CSSC. The $c_p(660)$ and $b_{bp}(555)$ were more related to the POC in HT waters than that in MT and LT waters, and $b_{bp}(555)$ was more related to the POC than $c_p(660)$ in HT waters, which were dominated by organic detritus (Table 2). Conversely, $c_p(660)$ was more related to POC than $b_{bp}(555)$ in LT waters, which were dominated by living phytoplankton (Table 2).

However, optical properties such as c_p and b_{bp} are usually not provided in satellite products because c_p and b_{bp} vary with the compositions of coastal waters. This leads to difficulties in defining their retrieval algorithms, especially in optically complex waters. Thus, we proposed multiple

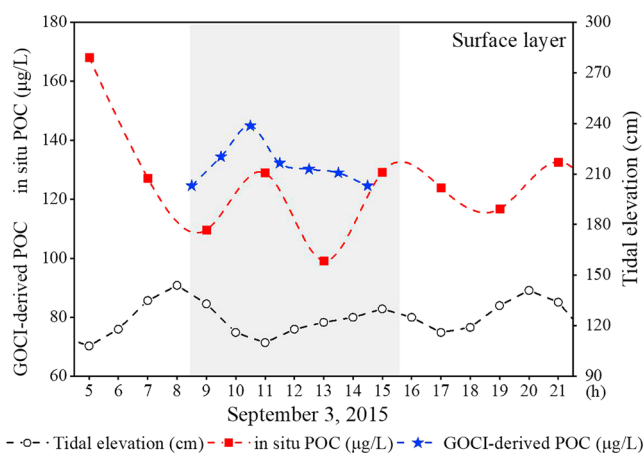


Figure 8. Diurnal variations in the surface layer at Station P in the Yellow River Estuary. The blue stars indicate the GOCI-derived POC concentrations, the red squares indicate the in situ POC concentrations, and the black circles denote the tidal elevation at the Dongyinggang tide gauge station (as shown earlier in Figure 1b). Only seven blue stars are present on 3 September 2015, due to heavy cloud cover. The shaded area signifies the time period of GOCI observations (8:30–15:30). GOCI = Geostationary Ocean Color Imager; POC = particulate organic carbon.

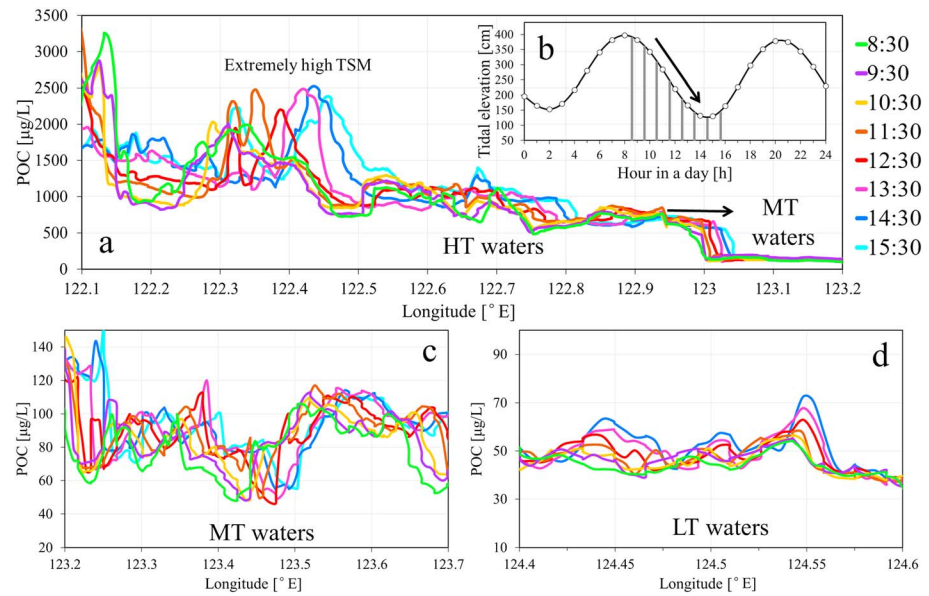


Figure 9. Diurnal variations in the Geostationary Ocean Color Imager-derived POC concentrations along the transect from A to B (marked with the white line in Figure 6a) on 7 April 2013, (a) in HT waters with the tidal elevations from the Lvhu tidal gauge station in (b) (marked with the white star in Figure 6a) on 7 April 2013; (c) typical MT waters and (d) typical LT waters. POC = particulate organic carbon; TSM = total suspended matter; HT = high-TSM; MT = moderate-TSM; LT = low-TSM.

optical proxies of POC corresponding to various water types (Table 3). From our in situ investigations, the TSM, Chla, and R_{rs} band ratio were regarded as POC proxy candidates for HT, MT, and LT waters, respectively, through correlation analysis (Figure 4 and Table 2).

HT waters occurred mainly in nearshore and estuary areas, and the POC in HT waters, which were highly impacted by river runoff, was the most related to TSM (Zhu et al., 2006). LT waters occurred mostly in off-shore areas, where the POC originates mainly from living organisms (mainly phytoplankton; Hung et al., 2013 ; Zhu et al., 2006). Table 2 indicates that the POC in LT waters had a good correlation with Chla.

Table 3
The Relationship Between POC and POC Proxy Parameters From In Situ Investigations

	Relationship	Sample	R^2	Area	Season	References
TSM	$POC = 6.068 \times TSM - 35.088$	20	0.99	Yellow Sea and the East China Sea	Spring	Jin et al. (2005)
Chla	$POC = 5.06 \times TSM + 37.33$	46	0.82	HT waters of the CSSC	February 2014 to September 2015	This study
	$POC = 162.18 \times Chla^{0.51}$	510	0.54	Global	All seasons	Legendre and Michaud (1999)
b_{bp}	$POC = 69.9 \times Chla^{0.63}$	57	0.72	LT waters of the CSSC	February 2014 to September 2015	This study
	$POC = 801.28 \times b_{bp}(532) - 4.81$	318	0.13	Baltic Sea	2008–2012	Simis et al. (2017)
c_p	$POC = 179.14 \times b_{bp}(555) + 74.7$	12	0.79	HT waters of the CSSC	February 2014 to September 2015	This study
	$POC = 326.6 \times c_p(660) + 2.0$	244	0.87	Gulf of Mexico (POC% > 25%)	November 1997 to August 2000	Son et al. (2009)
R_{rs}	$POC = 109.97 \times c_p(660) + 16.22$	53	0.52	LT waters of the CSSC	February 2014 to September 2015	This study
	$POC = 203.2 \times [R_{rs}(443)/R_{rs}(555)]^{-1.034}$	53	0.87	Eastern South Pacific Ocean and Atlantic Ocean	October–December 2004 and October–November 2005	Stramski et al. (2008)
	$POC = 10^{(6.36x^5 + 3.26x^4 - 0.37x^3 - 0.4x^2 + 1.79x + 2.42)}$	58	0.99	Gulf of Mexico	November 1997 to August 2000	Son et al. (2009)
	where $x = \frac{R_{rs}(555) - \max[R_{rs}(412), R_{rs}(443), R_{rs}(490)]}{R_{rs}(555) + \max[R_{rs}(412), R_{rs}(443), R_{rs}(490)]}$					
	$POC = 87.30 \times [R_{rs}(490)/R_{rs}(555)]^{-2.04}$	105	0.65	MT waters of the CSSC	February 2014 to September 2015	This study

Note. CSSC = continental shelf seas of China; POC = particulate organic carbon; TSM = total suspended matter; HT = high-TSM; MT = moderate-TSM; LT = low-TSM.

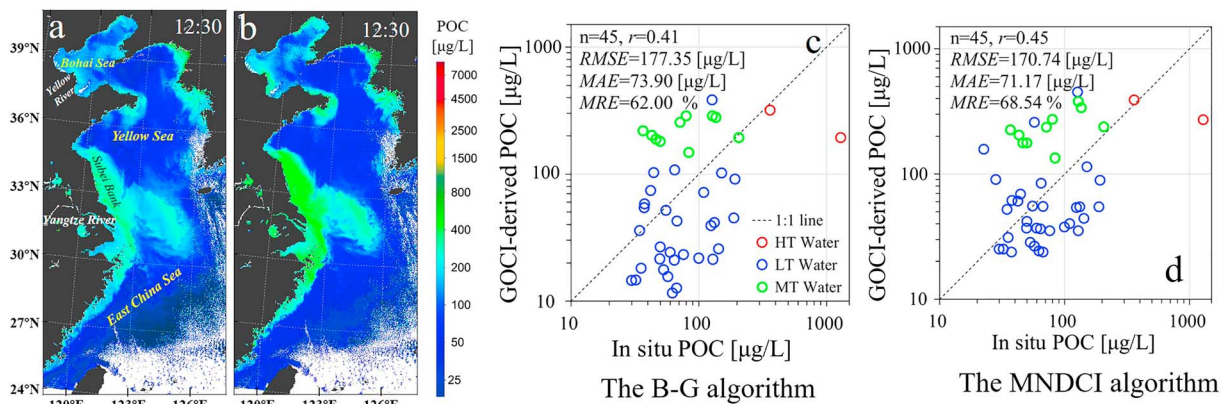


Figure 10. GOCI-derived POC imagery derived using the B-G algorithm (a) and the MNDCI algorithm (b) at 12:30 (Beijing time) on 7 April 2013, in the continental shelf seas of China. Validation of GOCI-derived POC using the B-G algorithm (c) and the MNDCI algorithm (d). Matchups from cruises for high-total suspended matter, middle-total suspended matter, and low-total suspended matter waters are marked with red circles, green circles, and blue circles, respectively. GOCI = Geostationary Ocean Color Imager; POC = particulate organic carbon; *RMSE* = root-mean-square error; *MAE* = mean absolute error; *MRE* = mean relative error.

The lowest POC value (approximately 50 $\mu\text{g/L}$ in Figure 6) was found in LT waters, partly due to the relatively low input from terrestrial sources, salinity, and intrusion of oligotrophic Kuroshio waters with low primary productivity (Zhu et al., 2006; Hung et al., 2013). Because MT waters occurred mainly in the mixing areas of HT and LT waters and contained both terrigenous organic POC and marine organic POC, neither TSM nor *Chla* was the optimal POC proxy. Indeed, it was found that the $R_{rs}(490)/R_{rs}(555)$ band ratio was the most related to the POC in MT waters and therefore constituted the optimal proxy for MT waters (Table 2).

6.2. Comparison of POC Retrievals Using Different Ocean Color Algorithms

The two POC retrieval algorithms (B-G and MNDCI) tuned for the CSSC waters were applied to the GOCI data. The results showed that the GOCI-derived POC values ranged from 300 to 500 $\mu\text{g/L}$ in the Yangtze River Estuary, the Yellow River Estuary and Subei Bank (Figures 10a and 10b), and these values were largely underestimated in comparison with the GOCI POC estimates from the POC_CSSC algorithm that ranged from 500 to 7,000 $\mu\text{g/L}$ (Figure 6e). Moreover, the spatial distribution of GOCI-derived POC concentrations from the B-G and the MNDCI algorithms did not exhibit a dramatic POC gradient from the estuaries to offshore areas. For HT waters, the POC estimated by the B-G algorithm (Figure 10a) was approximately 50 $\mu\text{g/L}$ lower than that derived from the MNDCI algorithm (Figure 10b).

The 1:1 lines in the scatter plots of the in situ POC versus the GOCI-derived POC matchup data demonstrate that the derived POC values were underestimated in the nearshore waters with a large bias and $RMSE = 177.35 \mu\text{g/L}$, $MAE = 73.9 \mu\text{g/L}$, and $MRE = 62.00\%$ for the B-G algorithm (Figure 10c) and $RMSE = 170.74 \mu\text{g/L}$, $MAE = 71.17 \mu\text{g/L}$, and $MRE = 68.54\%$ for the MNDCI algorithm (Figure 10d). This may be because the $R_{rs}(412)$ or $R_{rs}(443)$ used in the B-G and MNDCI algorithms are highly affected by CDOM and absorptive nonalgal particles in the blue spectral range in highly turbid waters and inherently contain large uncertainties from the atmospheric correction for turbid coastal waters (Le et al., 2017). For such waters, however, our POC_CSSC algorithm utilized longer wavebands to avoid these potential sources of errors. TSM was used as the proxy to estimate POC in HT waters, and TSM was retrieved using the SERT algorithm, which adopts R_{rs} in the red and near-infrared spectral ranges.

In addition, for the CSSC waters characterized by optical complexity, our POC_CSSC algorithm was based on the optical classification of water types; that is, the POC_CSSC algorithm adopted different surrogate parameters to retrieve POC for different water types. Such an approach can effectively improve the accuracy of the POC retrievals in the optically complex waters of the CSSC. The results demonstrate that the POC concentrations derived from our POC_CSSC algorithm can be more accurate than those derived from the B-G and MNDCI algorithms in the CSSC.

The POC_CSSC algorithm can also be applied to Sea-Viewing Wide Field-of-View Sensor, Moderate Resolution Imaging Spectroradiometer, and Medium Resolution Imaging Spectroradiometer satellite data

for POC retrievals. The TSM, R_{rs} , and Chla as proxies of remotely sensed POC in the POC_CSSC algorithm are general satellite ocean color products that can be obtained from various data centers; that is, Moderate Resolution Imaging Spectroradiometer products can be obtained from National Aeronautics and Space Administration, Medium Resolution Imaging Spectroradiometer products from the European Space Agency, and GOCI products from the Korea Ocean Satellite Center. Regarding the wavebands, the $R_{rs}(490)/R_{rs}(555)$ band ratio used in the POC_CSSC algorithm for MT waters uses common bands that are routinely measured by most ocean color sensors. Moreover, POC estimates obtained using the POC_CSSC algorithm in other regions with optically complex waters will also demonstrate a good accuracy if the algorithm is tuned by regional data sets.

6.3. Influence of Environmental Forcing on Diurnal POC Variation

According to our optical classification of water types, the Yangtze River Estuary was composed of HT waters (Figure 9a). Extremely high POC values (over approximately 2,000 $\mu\text{g/L}$) were found in the Yangtze River Estuary and its adjacent areas, that is, along the transect from 122.1°E to 122.5°E (Figure 9a), which correctly correspond to the maximum turbidity zone of the Yangtze River Estuary. The POC concentrations in HT waters were strongly correlated with TSM. The POC in the turbidity front along the transect from 123°E to 123.05°E showed a pronounced shift with the ebb tide, which also influenced the diurnal variation of TSM (Figure 9b). These findings are similar to the observations of Pan et al. (2018) for the diurnal TSM variation in the Yangtze River Estuary; that is, the diurnal TSM variation in the turbidity front is strongly controlled by tidal currents, while in the turbidity maximum zone, the variation is controlled by both runoff and tidal currents. Likewise, the study of (He et al., 2013) indicated via GOCI observations that TSM concentrations in the nearshore area of the CSSC have diurnal variability and that the diurnal TSM variation is caused mainly by tidal dynamics. Therefore, the diurnal POC variations may also be caused by tidal dynamics in HT waters. Furthermore, sediment discharge, wind, and hydrodynamic conditions may represent other factors related to TSM and POC variations over a relatively long time scale (e.g., over seasons or years; Qiu et al., 2017).

The GOCI observations (Figure 9d) revealed that high POC concentrations occurred mainly from approximately 12:30 to 14:30 in LT waters; this finding implies that the diurnal POC variation in LT waters may be related to the diurnal variation in phytoplankton abundance due to the diurnal variation in the solar illumination intensity. Sun et al. (2018) reported that the Chla concentration generally presents a maximum around noon, and the diurnal variation in Chla might result from the ability of phytoplankton to photosynthesize. In addition, these results imply that the POC may originate from local phytoplankton production and less from inputs of terrestrial organic matter.

Ultimately, the diurnal POC variations in the MT waters of the CSSC were complicated. This complexity might be affected by multiple dynamic and environmental factors. MT waters constitute a mixture of HT and LT waters, which may be influenced by terrestrial sources and phytoplankton release, respectively. In the future, it will be necessary to carry out in situ synthetic observations of multiple dynamic and environmental factors, including POC, in different water types to understand POC dynamics.

7. Conclusions

In this study, a large data set of matchups between biochemical parameters (POC, Chla, and TSM concentrations) and optical properties (c_p , b_{bp} , and R_{rs}) in the CSSC was obtained through six comprehensive cruises and then used to explore the optimal optical proxies for the POC to develop a remote sensing POC retrieval algorithm for various water types. The detailed findings in the CSSC were obtained as follows.

1. The CSSC waters were classified into three types (HT, MT, and LT waters) using a remote sensing optical classification algorithm. Three proxies, namely, TSM for HT waters, Chla for LT waters and $R_{rs}(490)/R_{rs}(555)$ for MT waters, were proposed for retrieving POC from remote sensing data. The validation results indicate that the POC retrieval accuracy ($RMSE = 42.11 \mu\text{g/L}$, $MAE = 29.35 \mu\text{g/L}$, and $MRE = 32.08\%$) of the proposed method was considerably better than that of the B-G band ratio algorithm and the MNDCI algorithm.
2. The GOCI-derived POC concentrations showed good agreement with the in situ time series observations with $MAE = 16.57 \mu\text{g/L}$ and $MRE = 15.29\%$. More broadly, the application of the POC_CSSC algorithm to

the GOCI satellite data revealed that tides exert a strong influence on POC, primarily in nearshore estuarine waters (HT waters) with high GOCI-observed POC concentrations (the water mass with a POC of 1,500–2,500 $\mu\text{g/L}$ progressively moved offshore). However, the offshore LT waters were less influenced by the tides than were the nearshore waters, demonstrating relatively low POC variability ($\sim 50 \mu\text{g/L}$), and the POC concentrations in the MT waters were influenced by both tides and other environmental factors.

Acknowledgments

This study is supported by the National Science Foundation of China project (41771378). We would like to express our gratitude to the 2014–2015 Oceanographic Research Vessel Sharing Program Committee of the National Natural Science Foundation of China, who allowed us to participate in the surveys conducted in the Yangtze Estuary, the Bohai Sea, the Yellow Sea, and the East China Sea. We would also like to thank all the scientists and staff members on the “Dongfanghong 2,” “Kexue 1,” and “Runjiang 1” research vessels for their assistance in the data acquisition. Last but not least, we would like to thank Professor Sun Jun of Tianjin University of Science and Technology, who provided the Chla data from the 201508YB survey used in this paper. We also thank Ying Cui from our laboratory for POC measurements. These data have supplemented the content of this paper. We are greatly indebted to Fang Cao for her help in improving and editing this manuscript. The GOCI images were provided by the Korea Ocean Satellite Center (http://kosc.kiost.ac.kr/eng/p10/kosc_p11.html). These data will be available via the China Ocean Science Data Sharing Service Platform, Estuary and Coastal Science Data Sharing Service Subcenter Platform. These data can be obtained by registered users via the link (<http://coastaldata.ecnu.edu.cn/figures-and-datasets-jgr-oceans-submission>).

References

- Allison, D. B., Stramski, D., & Mitchell, B. G. (2010). Empirical ocean color algorithms for estimating particulate organic carbon in the Southern Ocean. *Journal of Geophysical Research*, *115*, C10044. <https://doi.org/10.1029/2009JC006040>
- Bailey, S. W., & Werdell, P. J. (2006). A multi-sensor approach for the on-orbit validation of ocean color satellite data products. *Remote Sensing of Environment*, *102*(1–2), 12–23. <https://doi.org/10.1016/j.rse.2006.01.015>
- Balch, W. M., Bowler, B. C., Drapeau, D. T., Poulton, A. J., & Holligan, P. M. (2010). Biominerals and the vertical flux of particulate organic carbon from the surface ocean. *Geophysical Research Letters*, *37*, L22605. <https://doi.org/10.1029/2010GL044640>
- Boss, E., Guidi, L., Richardson, M. J., Stemann, L., Gardner, W., Bishop, J. K. B., et al. (2015). Optical techniques for remote and in-situ characterization of particles pertinent to GEOTRACES. *Progress in Oceanography*, *133*(Supplement C), 43–54. <https://doi.org/10.1016/j.pcean.2014.09.007>
- Bricaud, A., Morel, A., & Prieur, L. (1981). Absorption by dissolved organic matter of the sea (yellow substance) in the UV and visible domains. *Limnology and Oceanography*, *26*(1), 43–53. <https://doi.org/10.4319/lo.1981.26.1.0043>
- Cai, P., Zhao, D., Wang, L., Huang, B., & Dai, M. (2015). Role of particle stock and phytoplankton community structure in regulating particulate organic carbon export in a large marginal sea. *Journal of Geophysical Research: Oceans*, *120*, 2063–2095. <https://doi.org/10.1002/2014JC010432>
- Cetinić, I., Perry, M. J., Briggs, N. T., Kallin, E., D’Asaro, E. A., & Lee, C. M. (2012). Particulate organic carbon and inherent optical properties during 2008 North Atlantic Bloom Experiment. *Journal of Geophysical Research*, *117*, C06028. <https://doi.org/10.1029/2011JC007771>
- Chen, C. A. (2009). Chemical and physical fronts in the Bohai, Yellow and East China seas. *Journal of Marine Systems*, *78*(3), 394–410. <https://doi.org/10.1016/j.jmarsys.2008.11.016>
- Druffel, E. R. M., Williams, P. M., Bauer, J. E., & Ertel, J. R. (1992). Cycling of dissolved and particulate organic matter in the open ocean. *Journal of Geophysical Research*, *97*(C10), 15,639–15,659. <https://doi.org/10.1029/92JC01511>
- Fairall, C. W., Bradley, E. F., Rogers, D. P., Edson, J. B., & Young, G. S. (1996). Bulk parameterization of air-sea fluxes for Tropical Ocean-Global Atmosphere Coupled-Ocean Atmosphere Response Experiment. *Journal of Geophysical Research*, *101*(C2), 3747–3764. <https://doi.org/10.1029/95JC03205>
- Fargion, G. S., and Mueller, J. L. (2000). Ocean optics protocols for satellite ocean color sensor validation, Revision 2, National Aeronautics and Space Administration, Goddard Space Flight Center.
- Feng, H., Campbell, J. W., Dowell, M. D., & Moore, T. S. (2005). Modeling spectral reflectance of optically complex waters using bio-optical measurements from Tokyo Bay. *Remote Sensing of Environment*, *99*(3), 232–243. <https://doi.org/10.1016/j.rse.2005.08.015>
- Gardner, W. D., Mishonov, A. V., & Richardson, M. J. (2006). Global POC concentrations from in-situ and satellite data. *Deep Sea Research Part II: Topical Studies in Oceanography*, *53*(5–7), 718–740. <https://doi.org/10.1016/j.dsr2.2006.01.029>
- Gordon, H. R., & Wang, M. (1994). Retrieval of water-leaving radiance and aerosol optical thickness over the oceans with SeaWiFS: A preliminary algorithm. *Applied Optics*, *33*(3), 443–452. <https://doi.org/10.1364/AO.33.000443>
- He, X., Bai, Y., Pan, D., Huang, N., Dong, X., Chen, J., et al. (2013). Using geostationary satellite ocean color data to map the diurnal dynamics of suspended particulate matter in coastal waters. *Remote Sensing of Environment*, *133*, 225–239. <https://doi.org/10.1016/j.rse.2013.01.023>
- Hedges, J. I. (1992). Global biogeochemical cycles: Progress and problems. *Marine Chemistry*, *39*(1–3), 67–93. [https://doi.org/10.1016/0304-4203\(92\)90096-S](https://doi.org/10.1016/0304-4203(92)90096-S)
- Hedges, J. I., & Stern, J. H. (1984). Carbon and nitrogen determinations of carbonate-containing solids. *Limnology and Oceanography*, *29*(3), 657–663. <https://doi.org/10.4319/lo.1984.29.3.0657>
- Hu, S., Cao, W., Wang, G., Xu, Z., Lin, J., Zhao, W., et al. (2016). Comparison of MERIS, MODIS, SeaWiFS-derived particulate organic carbon, and in situ measurements in the South China Sea. *International Journal of Remote Sensing*, *37*(7), 1585–1600. <https://doi.org/10.1080/01431161.2015.1088673>
- Huang, C., Li, Y., Yang, H., Li, J., Chen, X., Sun, D., et al. (2014). Assessment of water constituents in highly turbid productive water by optimization bio-optical retrieval model after optical classification. *Journal of Hydrology*, *519*(B), 1572–1583. <https://doi.org/10.1016/j.jhydrol.2014.09.007>
- Hung, C. C., Tseng, C. W., Gong, G. C., Chen, K. S., Chen, M. H., & Hsu, S. C. (2013). Fluxes of particulate organic carbon in the East China Sea in summer. *Biogeosciences*, *10*(10), 6469–6484. <https://doi.org/10.5194/bg-10-6469-2013>
- Hung, J. J., Chen, C. H., Gong, G. C., Sheu, D. D., & Shiah, F. K. (2003). Distributions, stoichiometric patterns and cross-shelf exports of dissolved organic matter in the East China Sea. *Deep Sea Research Part II: Topical Studies in Oceanography*, *50*(6–7), 1127–1145. [https://doi.org/10.1016/S0967-0645\(03\)00014-6](https://doi.org/10.1016/S0967-0645(03)00014-6)
- Hung, J. J., Lin, P. L., & Liu, K. K. (2000). Dissolved and particulate organic carbon in the southern East China Sea. *Continental Shelf Research*, *20*(4–5), 545–569. [https://doi.org/10.1016/S0278-4343\(99\)00085-0](https://doi.org/10.1016/S0278-4343(99)00085-0)
- Jin, H. Y., Lin, Y. A., Chen, J. F., & Jin, M. M. (2005). Analysis of driving factors and distribution of particulate organic carbon in the Huanghai Sea and the East China Sea. *Acta Oceanologica Sinica [in Chinese with English abstract]*, *27*(5), 46–54.
- Knap, A. H., A. Michaels, A. R. Close, H. Ducklow, and A. G. Dickson (1996). Protocols for the joint Global Ocean Flux Study (JGOFS) Core Measurements, Bergen, Norway, JGOFS Report Nor.19, 170.
- Le, C., Lehrter, J. C., Hu, C., MacIntyre, H., & Beck, M. W. (2017). Satellite observation of particulate organic carbon dynamics on the Louisiana continental shelf. *Journal of Geophysical Research: Oceans*, *122*, 555–569. <https://doi.org/10.1002/2016JC012275>
- Le, C., Li, Y., Zha, Y., Sun, D., Huang, C., & Zhang, H. (2011). Remote estimation of chlorophyll a in optically complex waters based on optical classification. *Remote Sensing of Environment*, *115*(2), 725–737. <https://doi.org/10.1016/j.rse.2010.10.014>

- Legendre, L., & Michaud, J. (1999). Chlorophyll a to estimate the particulate organic carbon available as food to large zooplankton in the euphotic zone of oceans. *Journal of Plankton Research*, 21(11), 2067–2083. <https://doi.org/10.1093/plankt/21.11.2067>
- Li, X., Bianchi, T. S., Allison, M. A., Chapman, P., Mitra, S., Zhang, Z., et al. (2012). Composition, abundance and age of total organic carbon in surface sediments from the inner shelf of the East China Sea. *Marine Chemistry*, 145–147, 37–52. <https://doi.org/10.1016/j.marchem.2012.10.001>
- Liu, D., Keesing, J. K., Xing, Q., & Shi, P. (2009). World's largest macroalgal bloom caused by expansion of seaweed aquaculture in China. *Marine Pollution Bulletin*, 58(6), 888–895. <https://doi.org/10.1016/j.marpolbul.2009.01.013>
- Liu, Q., Pan, D., Bai, Y., Wu, K., Chen, C. A., Liu, Z., & Zhang, L. (2014). Estimating dissolved organic carbon inventories in the East China Sea using remote-sensing data. *Journal of Geophysical Research: Oceans*, 119, 6557–6574. <https://doi.org/10.1002/2014JC009868>
- Loisel, H., Nicolas, J., Deschamps, P., & Frouin, R. (2002). Seasonal and inter-annual variability of particulate organic matter in the global ocean. *Geophysical Research Letters*, 29(24), 2996. <https://doi.org/10.1029/2002GL015948>
- Loisel, H., Vantrepotte, C., Jamet, and D. N. Dinh (2013). Challenges and new advances in ocean color remote sensing of coastal waters, Chapter in oceanography research. InTech, 953–980,
- Lubac, B., & Loisel, H. (2007). Variability and classification of remote sensing reflectance spectra in the eastern English Channel and southern North Sea. *Remote Sensing of Environment*, 110(1), 45–58. <https://doi.org/10.1016/j.rse.2007.02.012>
- Maffione, R. A., & Dana, D. R. (1997). Instruments and methods for measuring the backward-scattering coefficient of ocean waters. *Applied Optics*, 36(24), 6057–6067. <https://doi.org/10.1364/AO.36.006057>
- Melin, F., Zibordi, G., Berthon, J., Bailey, S., Franz, B., Voss, K., et al. (2011). Assessment of MERIS reflectance data as processed with SeaDAS over the European seas. *Optics Express*, 19(25), 25,657–25,671. <https://doi.org/10.1364/OE.19.025657>
- Milliman, J. D., & Meade, R. H. (1983). World-wide delivery of river sediment to the oceans. *Journal of Geology*, 91(1), 1–21. <https://doi.org/10.1086/628741>
- Mobley, C. D. (1999). Estimation of the remote-sensing reflectance from above-surface measurements. *Applied Optics*, 38(36), 7442–7455. <https://doi.org/10.1364/AO.38.007442>
- Moore, T. S., Campbell, J. W., & Feng, H. (2001). A fuzzy logic classification scheme for selecting and blending satellite ocean color algorithms. *Ieee Transactions On Geoscience and Remote Sensing*, 39(8), 1764–1776. <https://doi.org/10.1109/36.942555>
- Pan, D., Liu, Q., & Bai, Y. (2014). Review and suggestions for estimating particulate organic carbon and dissolved organic carbon inventories in the ocean using remote sensing data. *Acta Oceanologica Sinica*, 33(1), 1–10. <https://doi.org/10.1007/s13131-014-0419-4>
- Pan, Y., Shen, F., & Verhoef, W. (2017). An improved spectral optimization algorithm for atmospheric correction over turbid coastal waters: A case study from the Changjiang (Yangtze) estuary and the adjacent coast. *Remote Sensing of Environment*, 191, 197–214. <https://doi.org/10.1016/j.rse.2017.01.013>
- Pan, Y., Shen, F., & Wei, X. (2018). Fusion of Landsat-8/OLI and GOCI data for hourly mapping of suspended particulate matter at high spatial resolution: A case study in the Yangtze (Changjiang) estuary. *Remote Sensing*, 10(2), 158. <https://doi.org/10.3390/rs10020158>
- Parsons, T. R. (1975). Particulate organic carbon in the sea. *Chemical Oceanography*, 14(2), 229–238. [https://doi.org/10.1016/0011-7471\(67\)90008-3](https://doi.org/10.1016/0011-7471(67)90008-3)
- Qiu, Z., Xiao, C., Perrie, W., Sun, D., Wang, S., Shen, H., et al. (2017). Using Landsat 8 data to estimate suspended particulate matter in the Yellow River estuary. *Journal of Geophysical Research: Oceans*, 122, 276–290. <https://doi.org/10.1002/2016JC012412>
- Ruddick, K. G., De Cauwer, V., Park, Y., & Moore, G. (2006). Seaborne measurements of near infrared water-leaving reflectance: The similarity spectrum for turbid waters. *Limnology and Oceanography*, 51(2), 1167–1179. <https://doi.org/10.4319/lo.2006.51.2.1167>
- Ryu, J. H., Choi, J. K., Eom, J., & Ahn, J. H. (2011). Temporal variation in Korean coastal waters using Geostationary Ocean Color Imager. *Journal of Coastal Research*, (642), 1731–1735.
- Sathyendranath, S., Stuart, V., Nair, A., Oka, K., Nakane, T., Bouman, H., et al. (2009). Carbon-to-chlorophyll ratio and growth rate of phytoplankton in the sea. *Marine Ecology Progress Series*, 383, 73–84. <https://doi.org/10.3354/meps07998>
- Shang, S., Wu, J., Huang, B., Lin, G., Lee, Z., Liu, J., & Shang, S. (2014). A new approach to discriminate dinoflagellate from diatom blooms from space in the East China Sea. *Journal of Geophysical Research: Oceans*, 119, 4653–4668. <https://doi.org/10.1002/2014JC009876>
- Shen, F., Salama, M. S., Zhou, Y., Li, J., Su, Z., & Kuang, D. (2010). Remote-sensing reflectance characteristics of highly turbid estuarine waters—A comparative experiment of the Yangtze River and the Yellow River. *International Journal of Remote Sensing*, 31(10), 2639–2654. <https://doi.org/10.1080/01431160903085610>
- Shen, F., Verhoef, W., Zhou, Y., Salama, M. S., & Liu, X. (2010). Satellite estimates of wide-range suspended sediment concentrations in Changjiang (Yangtze) estuary using MERIS data. *Estuaries and Coasts*, 33(6), 1420–1429. <https://doi.org/10.1007/s12237-010-9313-2>
- Shen, F., Zhou, Y., Li, D., Zhu, W., & Salama, M. S. (2010). Medium resolution imaging spectrometer (MERIS) estimation of chlorophyll-a concentration in the turbid sediment-laden waters of the Changjiang (Yangtze) Estuary. *International Journal of Remote Sensing*, 31(17–18), 4635–4650. <https://doi.org/10.1080/01431161.2010.485216>
- Shen, F., Zhou, Y., Peng, X., & Chen, Y. (2014). Satellite multi-sensor mapping of suspended particulate matter in turbid estuarine and coastal ocean, China. *International Journal of Remote Sensing*, 35(11–12), 4173–4192. <https://doi.org/10.1080/01431161.2014.916053>
- Simis, S. G. H., Ylostalo, P., Kallio, K. Y., Spilling, K., & Kutser, T. (2017). Contrasting seasonality in optical-biogeochemical properties of the Baltic Sea. *Plos One*, 12(4). <https://doi.org/10.1371/journal.pone.0173357>
- Siswanto, E., Tang, J., Yamaguchi, H., Ahn, Y., Ishizaka, J., Yoo, S., et al. (2011). Empirical ocean-color algorithms to retrieve chlorophyll-a, total suspended matter, and colored dissolved organic matter absorption coefficient in the Yellow and East China Seas. *Journal of Oceanography*, 67(5), 627–650. <https://doi.org/10.1007/s10872-011-0062-z>
- Sokoletsky, L. G., & Shen, F. (2014). Optical closure for remote-sensing reflectance based on accurate radiative transfer approximations: The case of the Changjiang (Yangtze) River Estuary and its adjacent coastal area, China. *International Journal of Remote Sensing*, 35(11–12), 4193–4224. <https://doi.org/10.1080/01431161.2014.916048>
- Son, Y. B., Gardner, W. D., Mishonov, A. V., & Richardson, M. J. (2009). Multispectral remote-sensing algorithms for particulate organic carbon (POC): The Gulf of Mexico. *Remote Sensing of Environment*, 113(1), 50–61. <https://doi.org/10.1016/j.rse.2008.08.011>
- Stramska, M., & Cieszynska, A. (2015). Ocean colour estimates of particulate organic carbon reservoirs in the global ocean - revisited. *International Journal of Remote Sensing*, 36(14), 3675–3700. <https://doi.org/10.1080/01431161.2015.1049380>
- Stramska, M., & Stramski, D. (2005). Variability of particulate organic carbon concentration in the north polar Atlantic based on ocean color observations with Sea-viewing Wide Field-of-view Sensor (SeaWiFS). *Journal of Geophysical Research*, 110, C10018. <https://doi.org/10.1029/2004JC002762>
- Stramski, D., Reynolds, R. A., Babin, M., Kaczmarek, S., Lewis, M. R., Röttgers, R., et al. (2008). Relationships between the surface concentration of particulate organic carbon and optical properties in the eastern South Pacific and eastern Atlantic Oceans. *Biogeosciences*, 5(1), 171–201. <https://doi.org/10.5194/bg-5-171-2008>

- Stramski, D., Reynolds, R. A., Kahru, M., & Mitchell, B. G. (1999). Estimation of particulate organic carbon in the ocean from satellite remote sensing. *Science*, *285*(5425), 239–242. <https://doi.org/10.1126/science.285.5425.239>
- Sun, D., Li, Y., Wang, Q., Gao, J., Lv, H., Le, C., & Huang, C. (2009). Light scattering properties and their relation to the biogeochemical composition of turbid productive waters: A case study of Lake Taihu. *Applied Optics*, *48*(11), 1979–1989. <https://doi.org/10.1364/AO.48.001979>
- Sun, X., Shen, F., Liu, D., Bellerby, R. G. J., Liu, Y., & Tang, R. (2018). In situ and satellite observations of phytoplankton size classes in the entire continental shelf sea, China. *Journal of Geophysical Research: Oceans*, *123*, 3523–3544. <https://doi.org/10.1029/2017JC013651>
- Tao, B., Mao, Z., Lei, H., Pan, D., Shen, Y., Bai, Y., et al. (2015). A novel method for discriminating *Prorocentrum donghaiense* from diatom blooms in the East China Sea using MODIS measurements. *Remote Sensing of Environment*, *158*(Supplement C), 267–280. <https://doi.org/10.1016/j.rse.2014.11.004>
- Wang, G. F., Cao, W. X., Yin, J. P., Zhou, W., Sun, Z. H., & Yang, Q. (2012). Progress on ocean-color remote sensing of particulate organic carbon. *Journal of Tropical Oceanography*, *31*(6), 48–56. <https://doi.org/10.3969/j.issn.1009-5470.2012.06.008>
- Wang, H., Wu, X., Bi, N., Li, S., Yuan, P., Wang, A., et al. (2017). Impacts of the dam-orientated water-sediment regulation scheme on the lower reaches and delta of the Yellow River (Huanghe): A review. *Global and Planetary Change*, *157*, 93–113. <https://doi.org/10.1016/j.gloplacha.2017.08.005>
- Wang, S., Chen, S., Qiu, Z., Sun, D., Zhang, H., Perrie, W., & Zhang, T. (2016). Variability in the backscattering efficiency of particles in the Bohai and Yellow Seas and related effects on optical properties. *Optics Express*, *24*(26), 29,360–29,379. <https://doi.org/10.1364/OE.24.029360>
- Ye, H., Li, J., Li, T., Shen, Q., Zhu, J., Wang, X., et al. (2016). Spectral Classification of the Yellow Sea and Implications for Coastal Ocean Color Remote Sensing. *Remote Sensing*, *8*(4), 321. <https://doi.org/10.3390/rs8040321>
- Yu, X., Salama, M. S., Shen, F., & Verhoef, W. (2016). Retrieval of the diffuse attenuation coefficient from GOCI images using the 2SeaColor model: A case study in the Yangtze Estuary. *Remote Sensing of Environment*, *175*, 109–119. <https://doi.org/10.1016/j.rse.2015.12.053>
- Zhang, J., Huang, D., Xiao, T., Liu, S. M., & Fang, J. (2016). Response of biogeochemical cycles and ecosystem in the East China Sea to multi-stressors introduction. *Deep Sea Research Part II: Topical Studies in Oceanography*, *124*, 1–5. <https://doi.org/10.1016/j.dsr2.2015.12.001>
- Zhang, X., Hu, L., Twardowski, M. S., & Sullivan, J. M. (2009). Scattering by solutions of major sea salts. *Optics Express*, *17*(22), 19,580–19,585. <https://doi.org/10.1364/OE.17.019580>
- Zhou, M., Shen, Z., & Yu, R. (2008). Responses of a coastal phytoplankton community to increased nutrient input from the Changjiang (Yangtze) River. *Continental Shelf Research*, *28*(12), 1483–1489. <https://doi.org/10.1016/j.csr.2007.02.009>
- Zhu, Z. Y., Zhang, J., Wu, Y., & Lin, J. (2006). Bulk particulate organic carbon in the East China Sea: Tidal influence and bottom transport. *Progress in Oceanography*, *69*(1), 37–60. <https://doi.org/10.1016/j.pocean.2006.02.014>